Long Noncoding RNA TINCR-Mediated Regulation of Acetyl-CoA Metabolism Promotes Nasopharyngeal Carcinoma Progression and Chemoresistance

Zi-Qi Zheng[1], Zhi-Xuan Li[1], Jia-Li Guan[1], Xu Liu[1], Jun-Yan Li[1], Yue Chen[1], Li Lin[1], Jia Kou[1], Jia-Wei Lv[1], Lu-Lu Zhang[2], Guan-Qun Zhou[1], Rui-Qi Liu[1], FoPing Chen[1], Xiao-Jun He[1], Ying-Qin Li[1], Feng Li[1], Si-Si Xu[1], Jun Ma[1], Na Liu[1], and Ying Sun[1]

ABSTRACT

Frontier evidence suggests that dysregulation of long noncoding RNAs (lncRNA) is ubiquitous in all human tumors, indicating that lncRNAs might have essential roles in tumorigenesis. Therefore, an in-depth study of the roles of lncRNA in nasopharyngeal carcinoma (NPC) carcinogenesis might be helpful to provide novel therapeutic targets. Here we report that lncRNA TINCR was significantly upregulated in NPC and was associated positively with poor survival. Silencing TINCR inhibited NPC progression and cisplatin resistance. Mechanistically, TINCR bound ACLY and protected it from ubiquitin degradation to maintain total cellular acetyl-CoA levels. Accumulation of cellular acetyl-CoA promoted *de novo* lipid biosynthesis and histone H3K27 acetylation, which ultimately regulated the peptidyl arginine deiminase 1 (PADI1)–MAPK–MMP2/9 pathway. In addition, insulin-like growth factor 2 mRNA-binding protein 3 interacted with TINCR and slowed its decay, which partially accounted for TINCR upregulation in NPC. These findings demonstrate that TINCR acts as a crucial driver of NPC progression and chemoresistance and highlights the newly identified TINCR–ACLY–PADI1–MAPK–MMP2/9 axis as a potential therapeutic target in NPC.

Significance: TINCR-mediated regulation of a PADI1–MAPK–MMP2/9 signaling pathway plays a critical role in NPC progression and chemoresistance, marking TINCR as a viable therapeutic target in this disease.

Introduction

Nasopharyngeal carcinoma (NPC), one of the most common cancers originating in the nasopharynx, is particularly prevalent in Southeastern Asia and North Africa (1). With the development of intensity-modulated radiotherapy and cisplatin-based concurrent chemotherapy, locoregional control of NPC has improved greatly (2). Distant metastasis, however, dominates the treatment failure of this disease. Recently, we reconfirmed the effectiveness of cisplatin-based induction chemotherapy in controlling distant failure and improving survival (3); however, patients with stable disease after induction chemotherapy, indicating resistance to this cisplatin-based therapy, were still at a high risk of distant recurrence (4). Thus, there is an urgent need to learn more about mechanisms of NPC metastasis and chemotherapy resistance to identify effective prognostic biomarkers and therapeutic strategies for NPC.

Recent high-profile reports have rekindled an interest in energy metabolism in cancer. The reprogramming of cellular energy metabolism, which fuels the metastasis and chemotherapy resistance of cancer cells, is regarded as a hallmark of cancer (5). Compared with nonmalignant cells, cancer cells not only show dysregulation of carbohydrates, but also have alterations related to lipid metabolism (6). Lipids are a class of metabolites that support cancer cell proliferation and metastasis, and have the ability to fight stress by providing energy, aiding the synthesis of macromolecules in membranes, and transducing lipid signals (7). Lipid biosynthesis from acetyl-CoA is the most common mechanism of lipid provision in neoplastic cells (8). Acetyl-CoA, located in both cytosol and nucleus, can directly link mitochondrial metabolism with nuclear and cytosolic processes, such as histone acetylation and lipid biosynthesis (9). However, it remains largely unknown how NPC cells reprogram lipid metabolism to support their malignant phenotypes.

To date, research has primarily focused on protein-coding genes to identify oncogenes or tumor suppressors that can be used as biomarkers and therapeutic targets for patients with NPC. However, protein-coding sequences account for less than 2% of the human genome. Among the various types of nonprotein-coding transcripts, a class referred to as long noncoding RNAs (lncRNA) has attracted increasing attention. Numerous lncRNAs are dysregulated in cancer cells that are resistant to chemotherapy, radiotherapy, and immunotherapy (10–12). However, the exact function and biological relevance of the vast majority of lncRNAs remain enigmatic. In recent years, several lncRNAs have been demonstrated to regulate cancer progression via participating in the cellular metabolism process. For example, lncRNA *EPB41L4A-AS1* was reported to suppress tumorigenesis by regulating

[1]State Key Laboratory of Oncology in South China, Collaborative Innovation Center of Cancer Medicine, Guangdong Key Laboratory of Nasopharyngeal Carcinoma Diagnosis and Therapy, Sun Yat-sen University Cancer Center, Guangzhou, People's Republic of China. [2]State Key Laboratory of Oncology in South China, Collaborative Innovation Center of Cancer Medicine, Department of Molecular Diagnostics, Sun Yat-sen University Cancer Center, Guangzhou, People's Republic of China.

Note: Supplementary data for this article are available at Cancer Research Online (http://cancerres.aacrjournals.org/).

Z.-Q. Zheng, Z.-X. Li, J.-L. Guan, and X. Liu contributed equally to this article.

Corresponding Authors: Ying Sun, Sun Yat-sen University Cancer Center, State Key Laboratory of Oncology in South China, Collaborative Innovation Center for Cancer Medicine, Guangdong Key Laboratory of Nasopharyngeal Carcinoma Diagnosis and Therapy, 651 Dongfeng Road East, Guangzhou 510060, People's Republic of China. Phone: 8602-0873-42253; Fax: 8602-0873-43295; E-mail: sunying@sysucc.org.cn; and Na Liu, liun1@sysucc.org.cn

Cancer Res 2020;80:5174–88

doi: 10.1158/0008-5472.CAN-19-3626

glycolysis and glutamine metabolism (13). Moreover, *LNMICC* promotes cervical cancer metastasis via reprogramming fatty acid metabolism (14). This strong evidence inspired us to explore the role of lncRNAs in the link between cell lipid metabolism and tumorigenesis in NPC.

In this study, by reanalyzing the lncRNA expression profile (GSE95166), we identified an oncogenic lncRNA, *TINCR*, which is markedly overexpressed in NPC and is associated with poor patient prognosis. Further study demonstrated that *TINCR* could promote NPC proliferation, metastasis, and cisplatin resistance by protecting ATP citrate lyase (ACLY) from ubiquitin degradation, upregulating acetyl-CoA levels, and ultimately promoting lipid biosynthesis via regulation of the peptidyl arginine deiminase 1 (PADI1)–MAPK–matrix metalloproteinase (MMP)2/9 pathway. In addition, we identified an oncofetal protein, insulin-like growth factor 2 mRNA-binding protein 3 (IGF2BP3), which could bind with *TINCR* and inhibit its RNA decay, which partially accounted for the elevated *TINCR* expression in NPC.

Materials and Methods

Clinical specimens

This study was approved by the Institutional Ethical Review Board of the Sun Yat-sen University Cancer Center (Guangzhou, China, GZR2020-134), and written informed consent was obtained from all patients. Twenty freshly frozen NPC and 16 normal nasopharynx tissues were obtained from Sun Yat-sen University Cancer Center (Guangzhou, China). NPC paraffin-embedded biopsy tissues (n = 216) were obtained from patients with detailed clinical characteristics and long-term follow-up data from January 2006 to December 2009.

Cell culture

The human immortalized nasopharyngeal epithelial cell lines NP69 and N2Tert were cultured in keratinocyte serum-free medium (Invitrogen) supplemented with bovine pituitary extract (BD Biosciences). The human NPC cell lines (CNE-1, CNE-2, HONE-1, SUNE-1, HNE-1, 5-8F, 6-10B, S18, S26, HK-1, and C666-1) were maintained in RPMI1640 (Invitrogen) or DMEM (Invitrogen) supplemented with 10% FBS (Gibco). All the cell lines had been authenticated and were generously provided by M. Zeng (Sun Yat-sen University Cancer Center, Guangzhou, China).

RNA extraction, reverse transcription, and quantitative PCR

Total RNA was isolated using TRIzol (Invitrogen), and the cDNA was synthesized using HiScript III RT SuperMix (Vazyme). Platinum SYBR Green qPCR SuperMix-UDG reagents (Invitrogen) were used for qRT-PCR analysis with the Bio-Rad CFX96 Touch sequence detection system (Bio-Rad Laboratories Inc.). The primers used for PCR are shown in Supplementary Table S1. The relative expression level was compared with that of *GAPDH* (encoding GAPDH) and fold changes were calculated using the $2^{-\Delta\Delta C_t}$ method.

Oligonucleotide transfection and generation of stably transfected cell lines

Lipofectamine 3000, RNAiMAX, or Opti-MEM I reagents (Invitrogen) were used for transient transfection. The siRNAs targeting *TINCR, ACLY*, or *IGF2BP3* were designed and synthesized by GenePharma (Supplementary Table S2). The short hairpin RNA plasmids against *TINCR* were synthesized according to the sequences shown in Supplementary Table S3. The sequence of *TINCR* and antisense-*TINCR* were synthesized by GENEWIZ and cloned into vectors pcDNA3.1(−) and pcDNA3.1(+), respectively (Addgene). The pENTER-*ACLY*, pENTER-*PADI1*, and pENTER-vector plasmids were purchased from Vigene Biosciences. The *TINCR* and HA-*ACLY* truncation expression constructs were constructed by cloning the truncated *TINCR* and *ACLY* cDNAs into vector pcDNA3.1(−); the primers used are listed in Supplementary Table S4.

To generate stably transfected cell lines, sh*TINCR* 2# was inserted into vector pLKO.1, and cotransfected into 293T cells with the psPAX2 packaging plasmid (Addgene) and pCMV-VSV-G plasmid (Addgene) using polyethyleneimine (Polysciences). After 24 hours, the cell supernatants were harvested to infect SUNE-1 cells, and the stable cell line was selected using puromycin and validated using qRT-PCR.

RNA sequencing and bioinformatic analysis

Total RNA of HONE-1 cells transfected with siRNAs against *TINCR* or *ACLY* was isolated to perform RNA sequencing (RNA-seq), which was carried out by BGI Genomics. The differentially expressed genes were subjected to Kyoto Encyclopedia of Genes and Genomes (KEGG) pathway analysis using the DAVID software. We also performed gene set enrichment analysis (GSEA) to identify biological functions enriched in NPC with *TINCR* knockdown. A threshold of $P < 0.05$ and a FDR ≤ 0.25 were used to select significant items.

Cell proliferation assay and cisplatin treatment

Transfected cells (1×10^3) were seeded in 96-well plates and cell viability was detected every 24 hours for 5 days using a Cell Counting Kit-8 (CCK-8) assay (Dojindo). For the colony formation assay, transfected cells were seeded in 6-well plates at a density of 400 cells per well, and incubated for approximately 10 days. The cells were then fixed, stained, and counted. In addition, 1×10^3 cells were incubated with cisplatin (0, 0.625, 1.25, 2.5, 5, and 10 μg/mL) for 72 hours and then subjected to a CCK-8 assay. For the clonogenic survival assay, 800 cells were treated with cisplatin (0, 4, and 8 μmol/L) for 2 hours and then cultured for approximately 10 days.

In vitro migration and invasion assays

Cell migration and invasion assays were carried out in Transwell chambers (Corning) coated without or with matrigel (BD Biosciences). Cells (5×10^4/1×10^5) suspended in 200 μL of serum-free medium were seeded in the upper chamber, and medium supplemented with 10% FBS was added to the lower chamber. After 12/24 hours, the cells that migrated/invaded to the lower surface of the membrane were fixed, stained, and observed.

RNA pull-down assay and mass spectrometry analysis

Full-length sense and antisense sequences of *TINCR* RNA and its fragments (1–876, 877–3733, 1–1815, 1816–3733, 1–3086, and 3087–3733) were transcribed *in vitro* using a MEGAscript T7 Transcription Kit (Thermo Fisher Scientific). The transcribed RNA was purified and labeled with biotin using a Pierce RNA 3′ End Desthiobiotinylation Kit (Thermo Fisher Scientific). The biotinylated RNAs were then incubated with cell lysates for a pull-down assay using a Pierce Magnetic RNA-Protein Pull-Down Kit (Thermo Fisher Scientific). The pulled down proteins were used for mass spectrometry (Huijun Biotechnology) or Western blotting analysis.

Western blotting

Total protein was extracted, separated, and transferred to polyvinylidene fluoride membranes (Millipore). The membranes were then blocked and incubated with primary antibodies against ACLY

(Abcam), β-actin (Abcam), HA-tag (Proteintech), acetyl-histone H3 (Lys27; Cell Signaling Technology), histone H3 (CST), *PADI1* (Biorbyt), *IGF2BP3* (Abcam), P38 MAPK (Cell Signaling Technology), phospho-P38 MAPK (Cell Signaling Technology), P44/42 MAPK (ERK1/2; Cell Signaling Technology), phospho-P44/42 MAPK (ERK1/2; Cell Signaling Technology), MMP2 (Bosterbio), and MMP9 (Bosterbio). After incubation with secondary antibodies, the bands were detected using chemiluminescence with the ChemiDoc MP Imaging System (Bio-Rad).

RNA immunoprecipitation assay

RNA immunoprecipitation (RIP) assays were performed using an EZ-Magna RIP Kit (Millipore). Briefly, cells were lysed and incubated with magnetic beads conjugated with anti-ACLY (Abcam; 5 μg), anti-IGF2BP3 (Proteintech; 5 μg), or anti-IgG (Millipore; 5 μg) antibodies for 6–8 hours at 4°C. Then, the beads with specific RNA-protein complex were collected and washes with RIP wash buffer. The coprecipitated RNAs were isolated by resuspending beads in TRIzol regent according to manufacturer's instructions and finally subjected to qRT-PCR.

FISH and immunofluorescence

FISH and immunofluorescence (IF) were performed to detect the colocalization of *TINCR* and ACLY or IGF2BP3. Briefly, cells were grown for 24 hours on glass slides. After fixation and permeabilization, the cells were incubated with *TINCR*-FISH Probe Mix (RiboBio), followed by anti-ACLY (Abcam; 1:20) or anti-IGF2BP3 antibodies (Abcam; 1:50). Thereafter, nuclei were stained with 4′,6-diamidino-2-phenylindole (DAPI; Sigma), and fluorescence images were obtained using a confocal scanning microscope (Olympus FV1000).

RNA electrophoretic mobility shift assay

RNA electrophoretic mobility shift assay (RNA-EMSA) was performed to study the binding region of the lncRNA with the target proteins (15). The biotin-labeled and nonlabeled probes that contained core structural area of *TINCR* (1–876 nt) were designed and synthesized by KeyGEN BioTECH. The human recombinant ACLY full-length protein was purchased from Abcam. RNA-EMSA was performed using a Chemiluminescent EMSA Detection Kit (KeyGEN BioTECH). Briefly, the probes were incubated with ACLY proteins only or ACLY proteins together with anti-ACLY antibodies. Then, the RNA-protein complexes were resolved on 5% native gels and subjected to autoradiography.

ELISA

ELISA was performed to determine the absolute molecular number of ACLY proteins in NPC cells. NPC cells with equal amount were harvested and lysed with RIPA buffer. Then, the absolute molecular number of ACLY proteins was detected by Human ACLY ELISA Kit (FineTest) in accordance with the manufacture's instruction.

In vivo ubiquitination and immunoprecipitation assay

Immunoprecipitation (IP) was performed to detect the ubiquitinated ACLY under native or denaturating condition in accordance with the previously reported protocols (16, 17). Briefly, cells were cotransfected with HA-labeled ubiquitin, pENTER-ACLY, and siRNAs targeting *TINCR* or its scrambled control. After 48 hours, the transfected cells were treated with MG132 (10 mmol/L) for 6 hours and then lysed with ice-cold IP lysis buffer with (Native-IP) or without (Denaturing-IP) 1% SDS. For Denaturing-IP, the cells lysates were denatured at 95°C for 5 minutes. A portion of cell lysates (∼10%) were saved for immunoblot analysis to detect the expression of target proteins, and the rest was diluted with 1 mL lysis buffer and sent for IP using anti-ACLY antibodies (Abcam; 5 μg) overnight at 4°C. Then, protein A/G Magnetic Beads (Thermo Fisher Scientific) were used to recover the immune complexes, which were washed with ice-cold IP buffer and heated at 95°C for 7 minutes for subsequent Western blotting analysis.

Metabolite measurements

Cells were seeded and then harvested using PIPA buffer (Millipore). Cell lysates were deproteinized using perchloric acid/KOH (BioVision, Milpitas), and used to determine the acetyl-CoA concentration using an acetyl-CoA Assay Kit (BioVision). For cholesterol measurement, cells were treated with chloroform: isopropanol:NP-40 (7:11:0.1), and the organic phase was separated, dried, and dissolved in Cholesterol Assay Buffer (BioVision). The total cholesterol levels were then determined using a Total Cholesterol and Cholesteryl Ester Assay Kit (BioVision). To measure free fatty acids, cells were treated with chloroform-Triton X-100 (1% Triton X-100 in pure chloroform), and the organic phase was separated, dried, and dissolved in Fatty Acid Assay Buffer (BioVision). The cellular free fatty acid levels were then determined using a Free Fatty Acid Quantification Colorimetric/Fluorometric Kit (BioVision).

UV-crosslinking immunoprecipitation sequencing

Crosslinking immunoprecipitation (CLIP) assay was performed in accordance with other protocols (18–21). Briefly, cells were irradiated once with 400 mJ/cm^2 and lysed in 500 μL cell lysis buffer and treated with Turbo DNase (5 μL; Life Technologies) and RNase T1 (20 μL; 1/50 for high RNase dilutions and 1/500 for low RNase dilutions). For IP, cell lysates were incubated with anti-IgG or anti-ACLY specific antibodies for 1 hour at room temperature, and then washed three times with high-salt wash buffer and once with PNK buffer. The IPed RNA was pre-treated with PNK reaction mixture (PNK-buffer, ATP, PNK and RNaseIn) and then labeled with biotinylated ADP using T4 RNA-ligation system (T4 RNA-ligase buffer, ATP, PEG 8000, biotinylated-ADP, and RNaseIn). Finally, the IPed RNA-protein complexes were eluted for RNA visualization, and the area of interest from the gel was eluted and sent for deep sequencing by RiboBio Corporation.

Chromatin immunoprecipitation

A chromatin immunoprecipitation (ChIP) assay was performed using a Pierce Magnetic ChIP Kit (Thermo Fisher Scientific). Briefly, cells were cross-linked with 1% formaldehyde, and quenched with 125 mmol/L glycine. The cells were then lysed, sonicated to yield 150–250 bp DNA fragments, and then immunoprecipitated with anti-acetyl-histone H3 (Lys27) antibodies (Cell Signaling Technology; 5 μg) or IgG. DNA was then isolated to perform ChIP sequencing (ChIP-seq), which was carried out by LC Science or for quantitative PCR. The input DNA and IgG were used for normalization and the primers are listed in Supplementary Table S5.

Zymography assay

Zymography assay was performed to test the proteolytic activity of MMP2 and MMP9 using a Gelatin Zymogram Analysis Kit (Wanlei-Bio). Briefly, conditioned medium (CM) standardized for cells number was mixed with an equal volume of nonreducing sample buffer and separated on 10% Novex Zymogram gel containing 0.1% gelatin. After

renaturation, the clear bands corresponding to proteolytic activity were detected by densitometry.

In vivo tumor growth and metastasis models

All animal procedures were approved by the Institutional Animal Care and Use Committee of Sun Yat-sen University Cancer Center (Guangzhou, China, L102012019030K). BALB/c nude mice (4–5 weeks old, female) were obtained from the Charles River Laboratories. For the tumor growth model, 1×10^6 SUNE-1 cells stably silenced for *TINCR* or control cells were injected into the armpits of mice. Once the tumor nodes became palpable ($\sim$100 mm^3), the mice were randomly divided into four groups ($n = 6$/group) and intraperitoneally injected with normal saline or cisplatin (DDP; 4 mg/kg) every 3 days. On day 30, the mice were sacrificed, and tumors were dissected and weighted. For the tumor metastasis model, 2×10^6 SUNE-1 cells stably silenced for *TINCR* or control cells were injected into the footpads of mice ($n = 8$/group). After 6 weeks, the mice were sacrificed, and their footpad tumors and inguinal lymph nodes were detached.

ISH

ISH was performed using an *in situ* hybridization detection Kit (Boster Biological Technology). The sequences of the probes against *TINCR* are listed in Supplementary Table S6. After digestion and prehybridization, sections were incubated with *TINCR*-specific probes for 16 hours at 37°C, and then incubated with rabbit antibodies against digoxin and biotinylated goat anti-rabbit secondary antibodies. Then, the sections were stained using streptavidin horseradish peroxidase, and visualized with 3,3′-diaminobenzidine.

IHC

Sections were deparaffinized, rehydrated, inactivated for endogenous peroxidase activity, subjected to antigen retrieval, blocked for nonspecific binding, and incubated with anti-ACLY (Abcam) or anti-pan-cytokeratin antibodies (Thermo Fisher Scientific) overnight at 4°C. IHC staining was visualized using the DAKO REAL EnVision Inspection System (DAKO).

Luciferase reporter assays

The sequence of full-length *TINCR* was amplified and cloned into vector pmir-GLO (Promega). Briefly, cells were plated in 6-well plate and cotransfected with pmirGLO-TINCR or its empty vector), together with siRNA targeting IGF2BP3 or its scrambled control using Lipofectamine 3000. The firefly luciferase activity in each well was measured with a Dual-Luciferase Reporter Assay System (Promega); the *Renilla* luciferase activity was used for normalization according to the manufacturer's protocol.

Statistical analysis

Student *t* test was used to compare groups. Comparisons among categorical variables were performed using χ^2 or Fisher exact tests. Survival curves were plotted using the Kaplan–Meier method and compared using log-rank tests. The significance of various variables for survival was analyzed using univariate and multivariate Cox regression analyses. Data are presented as the mean $\pm$ SD or the mean $\pm$ SEM. SPSS 22.0 (IBM Corp.) or GraphPad Prism (version 8.0, GraphPad Software, Inc.) were used for the statistical analyses. *P* values of < 0.05 were considered statistically significant. The sequencing data (RNA-seq, ChIP-seq, and CLIP sequencing) have been deposited in the National Center for Biotechnology Information's Gene Expression Omnibus (GEO; accession number GSE137977).

Results

TINCR is upregulated in NPC and correlates with poor prognosis

Reanalysis of the GEO dataset (GSE95166) revealed that *TINCR* was significantly upregulated in NPC tissues compared with that in normal tissues (**Fig. 1A**, $P < 0.01$). To verify this, we detected *TINCR* expression in 20 NPC and 16 normal nasopharynx tissues using qRT-PCR. As shown in **Fig. 1B**, *TINCR* expression was elevated in tumor tissues compared with that in normal tissues. In additional, we found that *TINCR* expression was much higher in 11 NPC cell lines than in NP69 and N2Tert cells (**Fig. 1C**). On the basis of The Cancer Genome Atlas (TCGA) database, we found that *TINCR* was upregulated in six other cancer types (Supplementary Fig. S1). These results indicated that *TINCR* might be an oncogene in multiple tumor types, including NPC.

We then investigated the prognostic value of *TINCR* with 216 paraffin-embedded NPC tissues using qRT-PCR. Stratifying patients with NPC according to the median expression value of *TINCR* (high-*TINCR* group = 108 and low-*TINCR* group = 108; **Fig. 1D**) produced Kaplan–Meier curves with significant differences in overall, disease-free, and distant-metastasis survival (**Fig. 1E–G**, all $P < 0.01$). Furthermore, high *TINCR* expression was significantly associated with a patient's locoregional failure, distant metastasis, and death. In addition, *TINCR* expression and tumor–node–metastasis (TNM) stage were independent indicators of prognosis (Supplementary Tables S7 and S8).

We further constructed a prognostic model with the combination of *TINCR* expression and TNM stage, and then classified patients into three separate groups: A low-risk group (low *TINCR* expression and early TNM stage, $n = 73$), an intermediate-risk group (high *TINCR* expression or advanced TNM stage, $n = 97$), and a high-risk group (high *TINCR* expression and advanced TNM stage, $n = 46$). Unsurprisingly, the overall, disease-free, and distant-metastasis survival rates were significantly different among the three groups (**Fig. 1H–J**, all $P < 0.01$). These results indicated that *TINCR* expression combined with clinical stage is a promising biomarker for NPC.

Silencing TINCR inhibits NPC proliferation, metastasis, and cisplatin resistance *in vitro*

To gain an insight into the function of *TINCR*, we first conducted RNA-seq in HONE-1 cells transfected with scrambled control or si-*TINCR*. Using three independent biological replicates, we identified 3,327 unique transcripts ($|\log_2$ fold-change$| > 1.5$ and $P < 0.01$), including 1,719 upregulated and 1,680 downregulated mRNAs (**Fig. 2A** and **B**). KEGG analysis indicated that these genes were enriched in cancer-related pathways (**Fig. 2C**). GSEA further revealed that the gene sets related to tumorigenesis, proliferation, metastasis, and cisplatin resistance were significantly positively correlated with *TINCR* expression (**Fig. 2D**; Supplementary Fig. S2).

To confirm these results, we conducted CCK-8 assays and found that compared with those transfected with the scrambled control, SUNE-1 and HONE-1 cells silenced for *TINCR* showed a substantially impaired proliferative capacity (**Fig. 2E**, all $P < 0.01$). Transwell migration and invasion assays showed markedly fewer migratory or invasive cells in the *TINCR* silencing group compared with those in the scrambled control group (**Fig. 2F**, all $P < 0.05$). Then, to assess the effect of *TINCR* on cisplatin (DDP) sensitivity, we exposed SUNE-1 and HONE-1 cells to a series of concentrations of DDP. CCK-8 and colony formation assays revealed that silencing *TINCR* increased the sensitivity of NPC cells to DDP (**Fig. 2G** and **H**, all $P < 0.05$). The opposite results were obtained when exogenously overexpressing

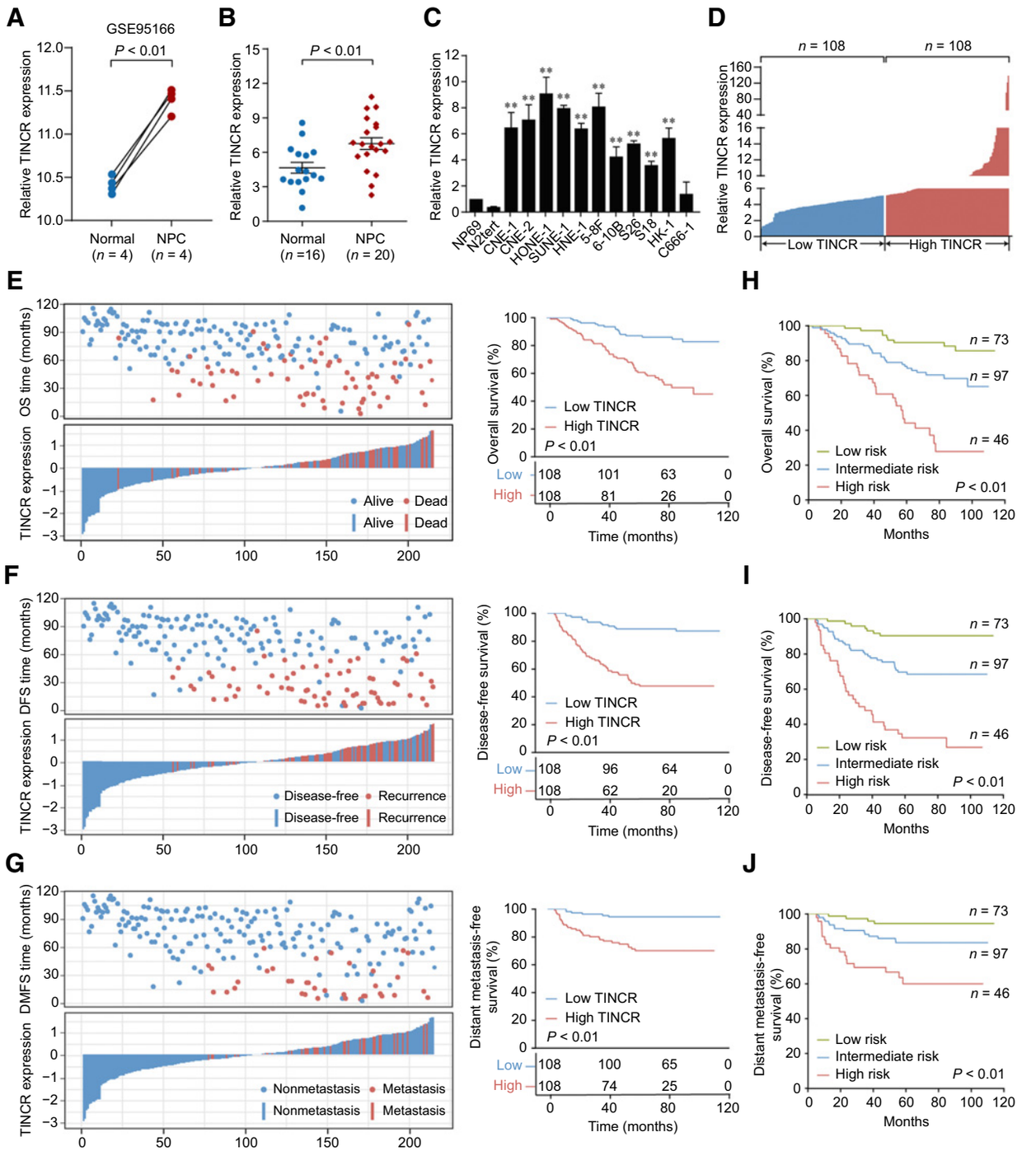

Figure 1.

TINCR is especially upregulated in NPC and correlates with poor prognosis. **A,** *TINCR* expression in three paired NPC and normal tissues based on microarray data (GSE95166). **B,** *TINCR* expression detected using qRT-PCR in normal nasopharynx ($n = 16$) and NPC ($n = 20$) tissues. **C,** *TINCR* expression in NPC cell lines and NP69 and N2Tert cells. **D,** *TINCR* expression in 216 paraffin-embedded NPC tissues. Patients with NPCs were divided into high ($n = 108$) or low ($n = 108$) *TINCR* expression groups according to the median expression level of *TINCR*. **E–G,** Kaplan–Meier curves for overall (**E**), disease-free (**F**), and distant metastasis-free survival (**G**) according to high or low *TINCR* expression. **H–J,** Kaplan–Meier analysis of overall (**H**), disease-free (**I**), and distant metastasis-free survival (**J**) according to the prognostic prediction model in patients with low (*TINCR* low expression and early TNM stage, $n = 73$), intermediate (*TINCR* high expression or advanced TNM stage, $n = 97$), and high (*TINCR* high expression and advanced TNM stage, $n = 46$) risk groups. Data are presented as the mean ± SEM. **, $P < 0.01$. The experiments were repeated independently at least three times.

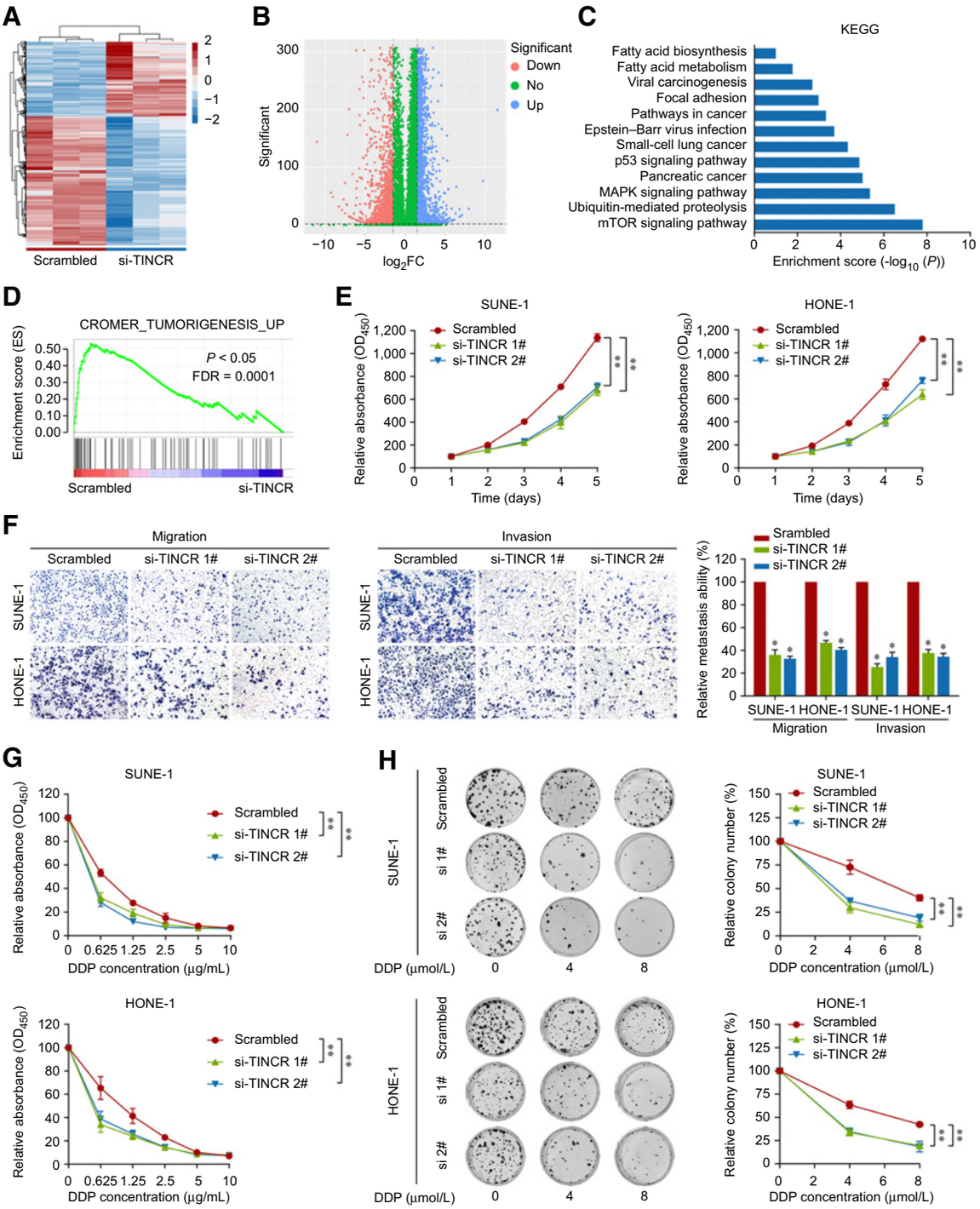

Figure 2.

Silencing *TINCR* inhibits NPC proliferation, metastasis, and cisplatin resistance *in vitro*. **A** and **B,** Heatmap (**A**) and volcano plot (**B**) illustrating the differently expressed genes in HONE-1 cells transfected with si-*TINCR* or the scrambled control. **C,** KEGG pathway analysis of genes regulated by *TINCR* in HONE-1 cells. Fatty acid metabolism, cancer, and protein ubiquitin degradation–related terms were among the significant pathways. **D,** The item "Tumorigenesis-related biological function" was enriched using GSEA in HONE-1 cells transfected with si-*TINCR* or the scrambled control. **E,** CCK-8 assays in SUNE-1 and HONE-1 cells transfected with si-*TINCR*s or the scrambled control. **F,** Representative images (left) and number (right) of migratory or invasive cells transfected with si-*TINCR*s or the scrambled control. **G,** CCK-8 assays determining the sensitivities of SUNE-1 and HONE-1 cells transfected with si-*TINCR*s or the scrambled control exposed to the indicated doses of cisplatin. **H,** Representative images (left) and number (right) of colonies formed in SUNE-1 and HONE-1 cells transfected with si-*TINCR*s or the scrambled control and treated with 0, 4, or 8 μmol/L cisplatin for 2 hours. Data are presented as the mean ± SD. *, $P < 0.05$; **, $P < 0.01$. The experiments were repeated independently at least three times.

TINCR (Supplementary Fig. S3A–S3E, all $P < 0.05$), and the phenotype induced by *TINCR* silencing could be rescued by restoring *TINCR* expression (Supplementary Fig. S4A–S4C, all $P < 0.05$). These findings indicated that *TINCR* promotes NPC proliferation and metastasis, and confers DDP chemoresistance on NPC cells.

TINCR directly interacts with ACLY

Recent studies report that certain lncRNAs exert their biological functions by interacting with proteins (22, 23). We performed an RNA pull-down assay followed by mass spectrometry and Western blot analysis (**Fig. 3A**), and identified ACLY as the most-enriched *TINCR*-interacting protein (Supplementary Tables S9 and S10; **Fig. 3B**). We then confirmed that the interaction of *TINCR* and ACLY was dose-dependent using biotin-*TINCR* pull-down lysates (**Fig. 3C**). Furthermore, we validated the association of *TINCR* with ACLY using RIP assay and found marked enrichment of *TINCR* using anti-ACLY antibodies rather than IgG (**Fig. 3D**, $P < 0.01$). FISH combined with IF staining revealed that the endogenous *TINCR* mainly colocalized with ACLY in the cytoplasm (**Fig. 3E**). These results suggested that *TINCR* could directly interact with ACLY.

To determine the specific region of *TINCR* that is responsible for its interaction with ACLY, we first predicted the secondary structure of *TINCR* using online software RNAfold (**Fig. 3F**). Then, we constructed different deletion transcripts of *TINCR* to perform RNA pull-down assays, and found that the binding efficiency of *TINCR* 1–876 nt to ACLY was the same as that of full-length *TINCR*. Further mapping of this region indicated that the 1–876 nt region was required for the *TINCR*–ACLY interaction (**Fig. 3G**), which was confirmed using an RNA-EMSA assay (**Fig. 3H** and **I**).

Moreover, to identify the domains of ACLY that interact with *TINCR*, we constructed four HA-tagged deletion mutants of ACLY (**Fig. 3J**; ref. 24). RNA pull-down assays showed that the A1 domain of ACLY, which contains the ATP-binding, citrate-binding, and CoA-binding regions, was required for *TINCR* binding (**Fig. 3K**), which was confirmed using RIP assay (**Fig. 3L**, $P < 0.01$). In addition, qRT-PCR and ELISA assays showed that there were about 700–800 *TINCR* RNAs per cell versus 4,500–6,000 ACLY proteins per cell in SUNE-1 and HONE-1 cells (Supplementary Fig. S5A–S5C), convincingly indicating the stoichiometric interaction of TINCR with ACLY. Taken together, these results suggest that the A1 (1–621 aa) domain of ACLY and nucleotides 1–876 nt of *TINCR* are critical for the *TINCR*–ACLY interaction.

TINCR inhibits ACLY ubiquitination degradation and regulates acetyl-CoA metabolism

An interesting point that arose from the experiment was that the protein level of ACLY decreased when *TINCR* was silenced, and increased in *TINCR* overexpression NPC cells (**Fig. 4A**). However, silencing or overexpression of *TINCR* had no impact on the transcription level of *ACLY* (**Fig. 4B**). LncRNAs have been reported to maintain the stability of their binding proteins by inhibiting their ubiquitination-mediated degradation (25–27); therefore, we treated SUNE-1 and HONE-1 cells with cycloheximide (a *de novo* protein synthesis inhibitor) and MG132 (a potent reversible cell-permeable proteasome inhibitor), respectively. The results showed that silencing *TINCR* led to a robust decrease in the ACLY protein level (**Fig. 4C**), and this reduction was rescued using MG132 (**Fig. 4D**), indicating that *TINCR* could protect ACLY from proteasome-dependent degradation. In agreement with this, we observed higher ACLY ubiquitination levels in *TINCR* knockdown cells (**Fig. 4E**; Supplementary Fig. S5D). These findings suggested that *TINCR* could maintain ACLY protein stability by inhibiting its ubiquitination-mediated degradation.

ACLY is a cytosolic homotetrameric enzyme that catalyzes the ATP-dependent conversion of citrate and CoA to oxaloacetate and acetyl-CoA, which is a precursor for lipid biosynthesis, including cholesterol, free fatty acids, and phospholipids (28–30). Meanwhile, the cellular acetyl-CoA pool is required for acetylation reactions in protein modification processes, such as histone acetylation (**Fig. 4F**). To investigate the biological impact of *TINCR*-mediated ACLY stabilization in NPC, we tested the *TINCR*-dependent changes in the cellular acetyl-CoA level. As expected, *TINCR* silencing led to corresponding decreases in the cellular acetyl-CoA level (**Fig. 4G**, $P < 0.01$), accompanied by decreased total cholesterol and free fatty acid levels (**Fig. 4H** and **I**, $P < 0.01$). Moreover, silencing *TINCR* led to a dramatic decrease in the global H3K27ac level without obviously affecting the expression of histone acetyltransferases KAT3A and KAT3B that was mainly responsible for H3K27ac (**Fig. 4J**; Supplementary Fig. S6A and S6B; ref. 31). These results indicated that *TINCR*-mediated ACLY stabilization could increase the cellular acetyl-CoA level to promote lipid synthesis and histone acetylation.

To further identify the specific motifs that are responsible for ACLY binding, we also conducted UV- CLIP sequencing. Consistent with the previous findings, we identified the 1-876nt of TINCR as the main region responsible for binding ACLY protein, with the short sequence motif CUGKR (K corresponds to G or U; R corresponds to G or A) at the end of this fragment (Supplementary Fig. S7A and S7B). In addition, we performed rescue experiments by overexpressing wild-type TINCR (TINCR-WT), ACLY-binding motifs mutant or deletion TINCR (TINCR-Mut/TINCR-Del) in HONE-1 cells with TINCR knockdown. Western blot analysis and metabolic molecule analysis revealed that silencing TINCR significantly inhibited ACLY protein expression and cellular lipid synthesis levels, which could be partially restored by exogenous add-back of full-length TINCR transcripts (TINCR-WT), but not the motifs deficient TINCR transcripts (mutant or deletion; Supplementary Fig. S7C and S7D). These results revealed the functional and molecular importance of CUGKR motif for TINCR–ACLY interaction.

Acetyl-CoA is responsible for TINCR-mediated NPC progression and chemoresistance

To determine whether an increased acetyl-CoA level is required for *TINCR*-mediated NPC progression and chemoresistance, we performed rescue experiments by increasing the cellular acetyl-CoA level using acetate, because acetyl-CoA is a membrane-impermeant molecule (32, 33). As expected, the reduction in cellular acetyl-CoA, cholesterol, and free fatty acid levels induced by *TINCR* silencing was reversed after acetate supplementation, in a dose-dependent manner (Supplementary Fig. S8A, $P < 0.05$). Moreover, H3K27ac levels were dramatically decreased when treated with C646 (a histone acetyltransferase inhibitor), which became more obvious under *TINCR* silencing. This phenomenon was rescued by supplementation with acetate (Supplementary Fig. S8B). Meanwhile, acetate supplementation significantly reversed the suppression of proliferation, metastasis, and chemoresistance induced by *TINCR* silencing (Supplementary Fig. S8C–S8F, $P < 0.01$). These results indicated that an increase in acetyl-CoA levels is required for the oncogenic role of *TINCR* in NPC.

TINCR leads to epigenetic activation of PADI1 expression

To identify the downstream genes involved in *TINCR*–ACLY–acetyl-CoA–mediated histone acetylation modification, we performed RNA-seq in HONE-1 cells, with or without *TINCR* or *ACLY* silencing,

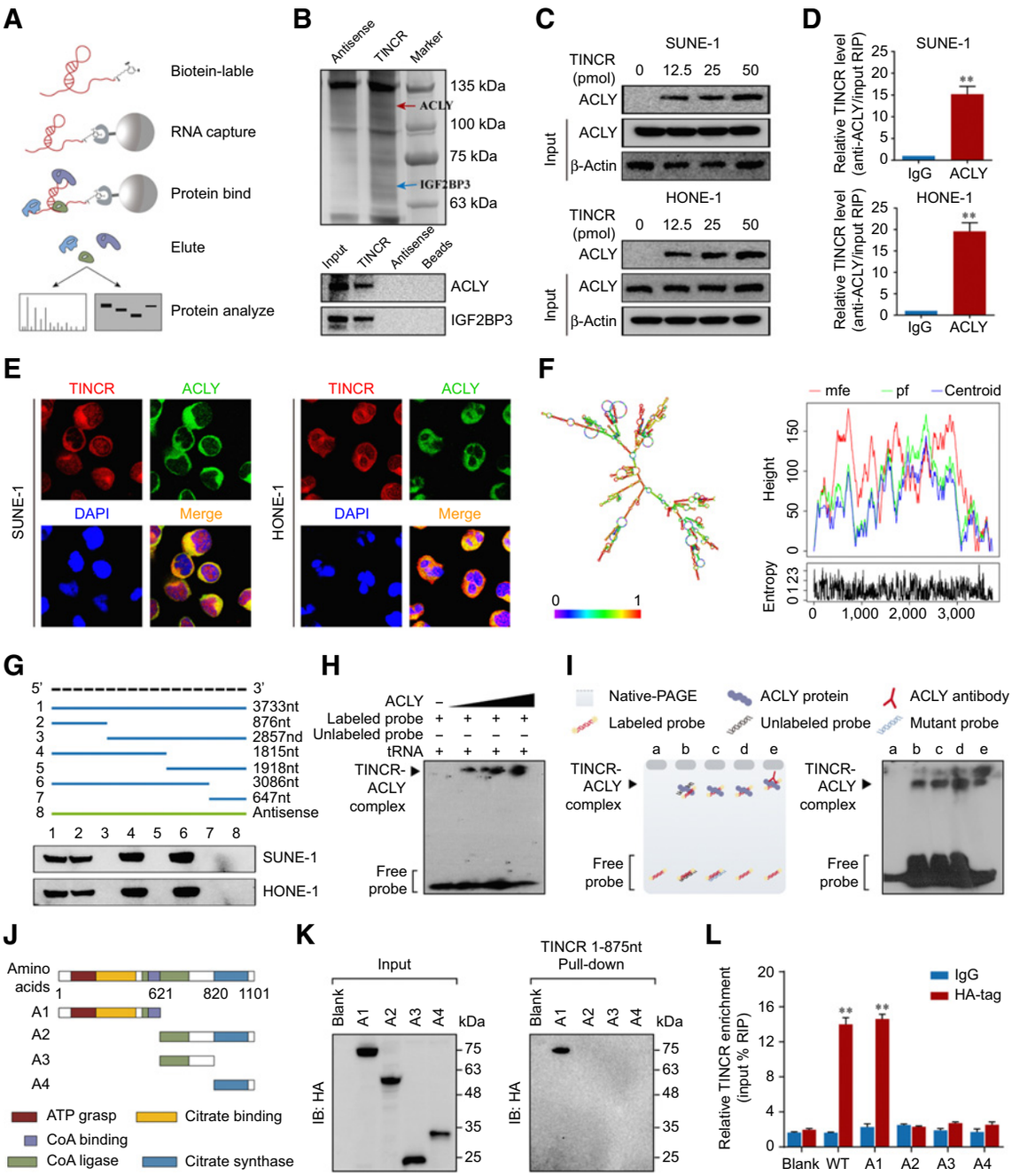

Figure 3.

TINCR directly interacts with ACLY. **A,** Schematic diagram of the RNA pull-down assay used to identify the proteins that bound to *TINCR*. **B,** Silver staining of biotinylated *TINCR*-associated proteins, and the specific bands that were excised for mass spectrometry (top) and Western blot (bottom) analysis. The arrows indicate ACLY (red) and IGF2BP3 (blue) proteins as the unique bands for *TINCR*. **C,** Western blotting analysis of the interaction of ACLY and *TINCR* from the RNA pull-down assay. **D,** RIP assay was performed using anti-ACLY antibodies to detect *TINCR* enrichment in the immunoprecipitated complexes. **E,** FISH and IF assays showing that *TINCR* (Cy3; red) and ACLY (green) are mainly colocalized in the cytoplasm. Nuclei, blue (DAPI). **F,** The predicted secondary structure (left) and mountain plot (right) representing the MFE (red), thermodynamic ensemble of RNA (green), and centroid (blue) structures of *TINCR*. **G,** Deletion mapping of the ACLY-binding domain in *TINCR*. Top, diagrams of full-length *TINCR* and its deletion fragments. Bottom, Western blotting analysis for ACLY pulled down by different *TINCR* constructs. **H,** Different concentrations of ACLY protein incubated with biotin-labeled *TINCR* (1–876 nt) probes for an EMSA assay. **I,** Schematic representation (left) and respective image (right) of the EMSA assay, showing that ACLY could bind to *TINCR* 1–876 nt. **J,** Schematic representation of plasmids-expressing HA-tagged wild-type or deletion mutants of *ACLY*. **K,** Western blotting analysis of the HA-tagged wild-type or deletion mutants of ACLY retrieved by *in vitro*-transcribed biotin-labeled *TINCR*. **L,** RIP assay was performed to detect *TINCR's* association with the ACLY domain. Data are presented as the mean ± SD. **, $P < 0.01$. The experiments were repeated independently at least three times.

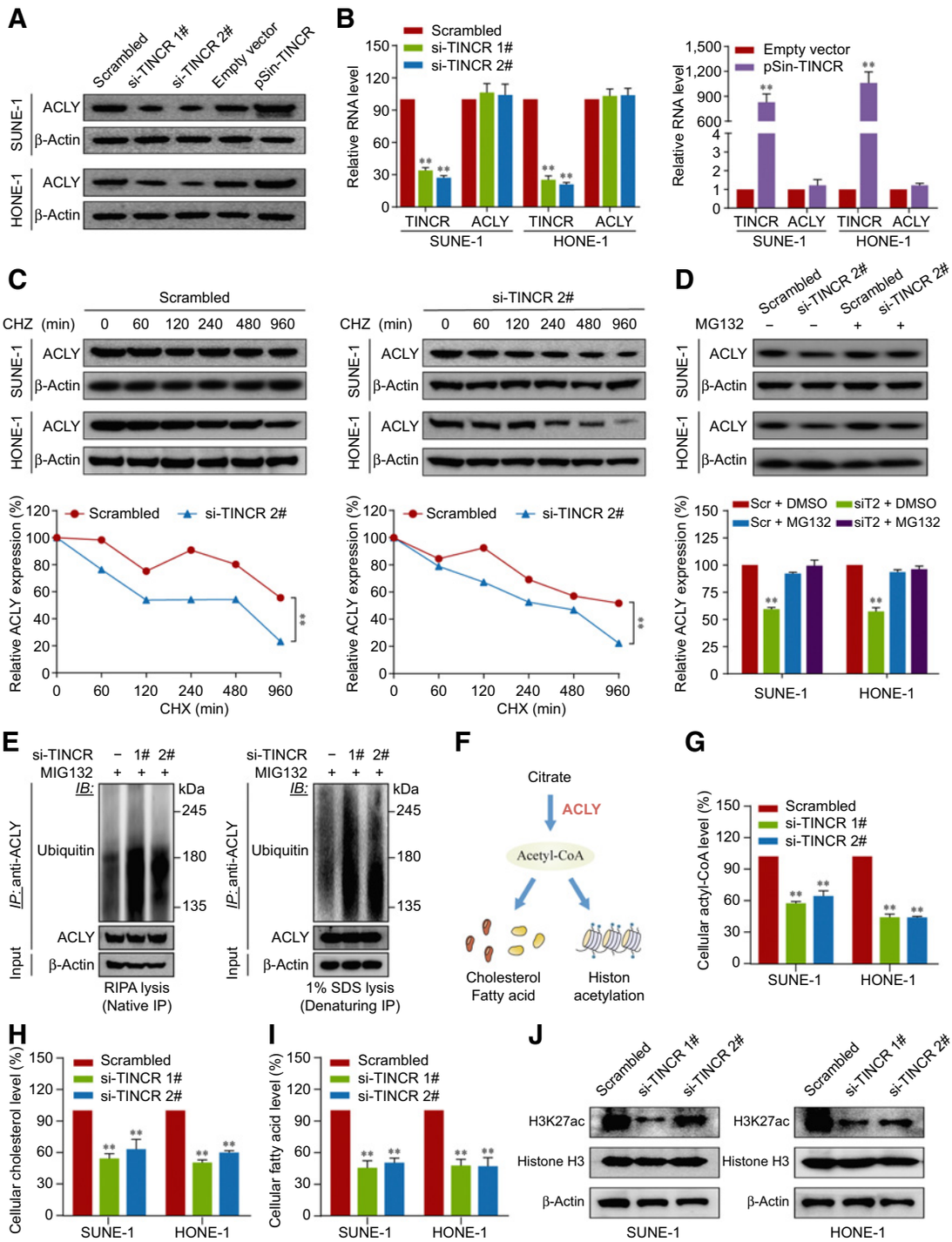

Figure 4.

TINCR inhibits ACLY ubiquitination degradation and regulates acetyl-CoA metabolism. **A** and **B,** Western blotting (**A**) and qRT-PCR (**B**) analysis of ACLY and TINCR expression levels in SUNE-1 and HONE-1 cells transfected as indicated. **C,** Representative images (top) and statistical analysis (bottom) of ACLY protein levels in SUNE-1 and HONE-1 cells transfected with si-*TINCR* 2# or the scrambled control under treatment with 50 μg/mL cycloheximide (CHX) for the indicated times. **D,** Representative images (top) and statistical analysis (bottom) of ACLY protein levels in SUNE-1 and HONE-1 cells transfected with si-*TINCR* 2# or the scrambled control under treatment, with or without proteasome inhibitor MG132 (10 μmol/L). **E,** The effects of silencing *TINCR* on the ubiquitination of ACLY in SUNE-1 cells. Immunoprecipitated ACLY was compared under native (IP lysis buffer) and denaturing (IP lysis buffer containing 1% SDS) lysis conditions. **F,** Metabolism diagram of cellular acetyl-CoA in mammalian cells, in which *ACLY* is responsible for acetyl-CoA generation. **G–J,** Levels of total acetyl-CoA (**G**), cholesterol (**H**), free fatty acids (**I**), and H3K27ac (**J**) in SUNE-1, and HONE-1 cells transfected with si-*TINCR*s or the scrambled control. Data are presented as the mean ± SD. **, $P < 0.01$. The experiments were repeated independently at least three times.

as well as H3K27ac ChIP-seq in HONE-1 cells, with or without *ACLY* silencing. Taking the intersection, we found two potential downstream genes, *CYB5R2* (encoding cytochrome b5 reductase 2) and *PADI1* (encoding peptidyl arginine deiminase 1; **Fig. 5A**). qRT-PCR confirmed the reduction of *CYB5R2* and *PADI1* after *TINCR* knockdown, with *PADI1* showing a more obvious decrease (**Fig. 5B**). In addition, a positive correlation between *TINCR* and *PADI1* expression was found in 20 frozen NPC tissues (**Fig. 5C**; Pearson $r = 0.656$, $P < 0.01$), which was also found in 16 other types of cancers, based on TCGA database analysis (Supplementary Fig. S9, $P < 0.01$). Furthermore, we found that the recruitment of H3K27ac to the *PADI1* promoter decreased dramatically when *TINCR* was silenced (**Fig. 5D**, $P < 0.01$). These results indicated that *TINCR* could upregulate *PADI1* by promoting the H3K27ac level at the *PADI1* promoter region.

PADI1 was reported to promote cancer metastasis via the MAPK–MMP2/9 pathway (34); therefore, we assessed the expression levels of PADI1, MMP2, and MMP9 in SUNE1 and HONE1 cells with TINCR silencing and observed that they were decreased. These inhibitory effects could be abolished by restoring *ACLY* expression. Meanwhile, the phosphorylation levels of P38 MAPK and ERK1/2 that were induced by *TINCR* silencing were abolished by restoring *ACLY* expression (**Fig. 5E**). In addition, silencing *TINCR* decreased the proteolytic activities of MMP2/9 in CM of NPC cells, but had no effects on H3K27ac levels at MMP2/9 promoters (Supplementary Fig. S10A–S10C). More importantly, the suppressive effects on NPC proliferation and metastasis, and chemoresistance induced by *TINCR*-silencing were partially rescued by restoration of *PADI1* (**Fig. 5F–I**). These results demonstrated that *PADI1* is a functional mediator of *TINCR* in NPC.

Silencing TINCR impairs NPC proliferation, metastasis, and cisplatin resistances *in vivo*

To characterize the oncogenic function of *TINCR in vivo*, we inoculated SUNE-1 cells with or without *TINCR* silencing into the armpit of nude mice to construct a xenograft mouse model. The tumor size, volume, and weight in *TINCR*-silenced group were dramatically reduced compared with those in the control group. Moreover, the tumors in *TINCR*-silenced group were much more sensitive to cisplatin treatment (**Fig. 6A–C**, $P < 0.01$). Further analysis showed that knockdown of *TINCR* resulted in a reduction in *ACLY* expression and acetyl-CoA levels (**Fig. 6D–F**, $P < 0.05$). In addition, we built an inguinal lymph node metastatic model (**Fig. 6G**) as reported previously (35), and found that both the volumes of the primary foot pad tumors and metastatic inguinal lymph nodes were smaller in the *TINCR*-silenced group than in the control group (**Fig. 6H**). Tumors in the *TINCR*-silenced group had a less aggressive phenotype with invasion toward the muscle (**Fig. 6I**). The inguinal lymph node metastasis ratio was markedly lower in *TINCR*-silenced group (**Fig. 6J** and **K**, $P < 0.05$). These data implied that *TINCR* could promote NPC cell proliferation, metastasis, and cisplatin resistance *in vivo*.

IGF2BP3 interacts with TINCR and slows down its RNA decay

To further explore the upstream mechanism of *TINCR* upregulation in NPC, we reanalyzed our RNA pull-down results and found that *TINCR* might also interact with IGF2BP3(**Fig. 3B**), a well-known RNA-binding protein reported to regulate the translation, localization, or stability of its target RNAs (36–38). The interaction of *TINCR* and IGF2BP3 was confirmed using biotin-*TINCR* pull-down samples (**Fig. 7A**). RIP assay implied that the enrichment of *TINCR* in complexes precipitated with anti-IGF2BP3 antibodies was much higher than that gained using IgG (**Fig. 7B**; $P < 0.01$). *TINCR* and IGF2BP3 are mainly colocalized in the cytoplasm (**Fig. 7C**). These results suggested that *TINCR* could interact with IGF2BP3.

Furthermore, we found that interference with *TINCR* expression had no effect on IGF2BP3 expression (Supplementary Fig. S11A). However, knockdown of *IGF2BP3* led to a dramatic decrease in *TINCR* levels (**Fig. 7D** and **E**, $P < 0.01$). *IGF2BP3* was significantly upregulated in NPC tissues, which was verified in the GEO dataset (GSE12452; Supplementary Fig. S11B and S11C, $P < 0.01$). More importantly, a positive correlation between *IGF2BP3* and *TINCR* expression was observed (**Fig. 7F**). Then, we specifically blocked RNA Polymerase II transcription using α-amanitin (50 μmol/L) as described previously (39), and found that silencing *IGF2BP3* promoted *TINCR* degradation (**Fig. 7G**, all $P < 0.01$). Luciferase reporter assays showed that silencing *IGF2BP3* led to a dramatic decrease of luciferase activity in cells transfected with the full-length *TINCR* plasmid (**Fig. 7H**, $P < 0.01$). These results revealed that IGF2BP3 slows down *TINCR* RNA decay, which may partially account for *TINCR*'s upregulation in NPC.

Taken together, we proposed a model in which IGF2BP3 stabilizes *TINCR* to protect ACLY from ubiquitin degradation, which upregulates acetyl-CoA levels, and promotes lipid biosynthesis and histone acetylation by activating the PADI1–MAPK–MMP2/9 pathway, ultimately promoting NPC proliferation, metastasis, and cisplatin resistance (**Fig. 7I**).

Discussion

To understand the mechanisms underlying NPC carcinogenesis and chemoresistance, a large number of genetic and epigenetic profiling studies have been conducted in recent years (40). Among them, lncRNAs have attracted attention because of their participation in several cancer-associated processes, including epigenetic regulation, DNA damage, cell-cycle regulation, cell survival, cell metabolism, and signal transduction pathways (41). However, the clinical significance of lncRNAs and their regulatory mechanisms in NPC remain unclear. In this study, we identified an oncogenic lncRNA *TINCR*, which was first identified to regulate differentiation genes in epidermal tissue (42). Subsequently, *TINCR* was reported to promote carcinogenesis in gastric and colorectal (43, 44), indicating that *TINCR* might play an essential role in the occurrence and development of various tumors. We found subsequently that *TINCR* promotes NPC cell proliferation, metastasis, and cisplatin resistance by maintaining *ACLY* protein levels and regulating the cellular acetyl-CoA level.

Energy and macromolecules are necessary for cancer cells to maintain their high proliferation rates (45). *ACLY* is a cytosolic enzyme responsible for acetyl-CoA synthesis in the *de novo* lipogenesis pathway, and has been reported to be aberrantly upregulated in cancer cells (46). Acetyl-CoA is a precursor for both lipids and the mevalonate synthesis pathways (47), where lipids are responsible for energy supply, highly active membrane biosynthesis, and signaling (48), thereby promoting carcinogenesis and cancer development. In contrast, acetyl-CoA is required for acetylation reactions, especially histone acetylation in the nucleus. Histone acetylation–modified proteins are critical for regulating global chromatin architecture and gene transcription (49). As such, *ACLY*-mediated energy metabolism and histone acetylation provide supporting for cancer tumorigenesis and development. *ACLY* was identified as a potential anticancer target in 2005, through inhibiting its metabolic activity by genetic methods or using a chemical inhibitor SB-204990 (50). To the best of our knowledge, *TINCR* represents the first lncRNA that links acetyl-CoA metabolism to NPC carcinogenesis.

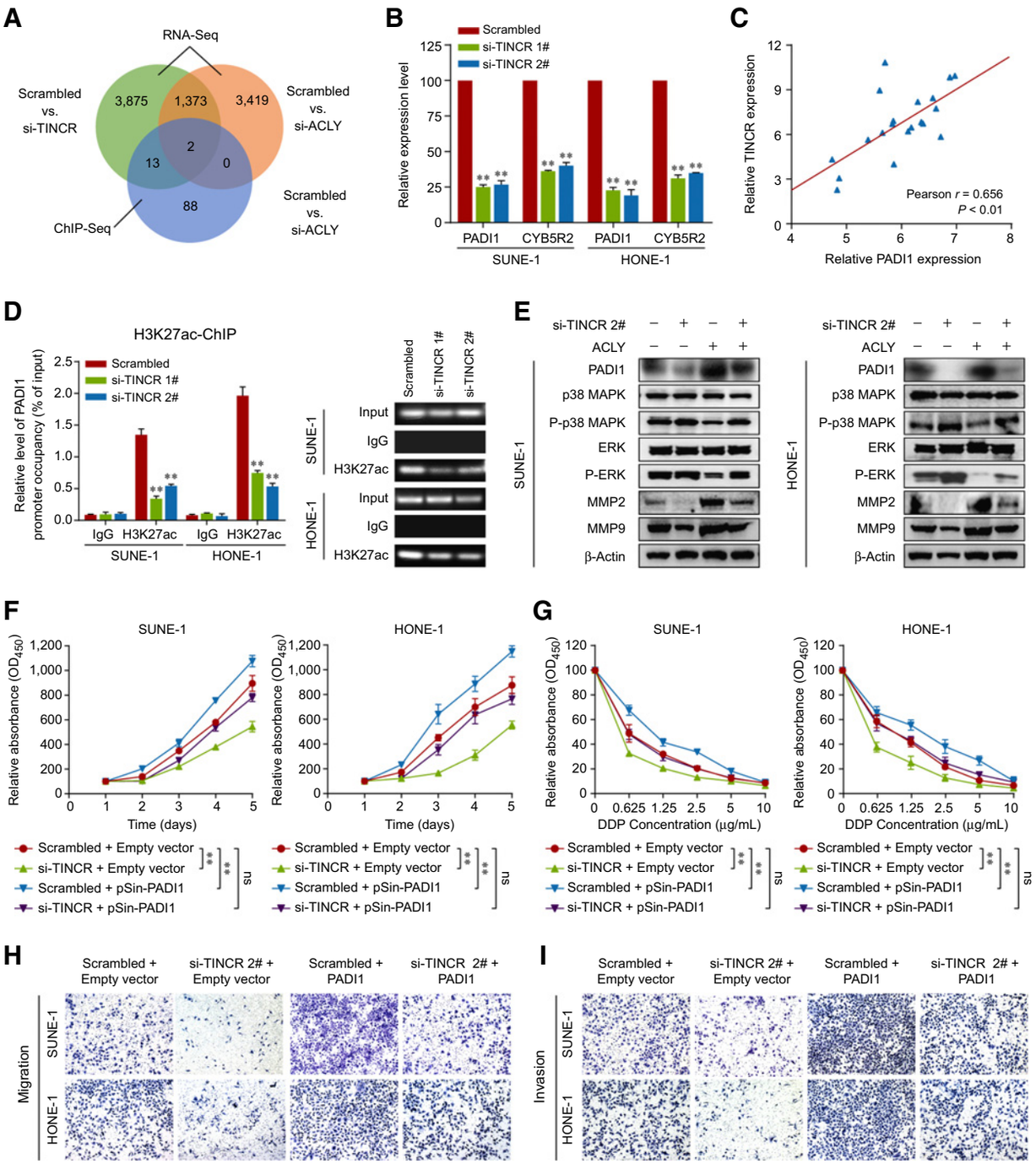

Figure 5.

TINCR leads to epigenetic activation of PADI1 expression. **A,** Overall analysis of RNA-seq and ChIP-seq data in the indicated cell lines. Overlapping gene sets identified among the downregulated genes after silencing of *TINCR* (left) or *ACLY* (right) and less enriched genes in the H3K27ac ChIP assay of HONE-1 cells with *ACLY* silencing. **B,** qRT-PCR analysis of *PADI1* and *CYB5R2* expression in SUNE-1 and HONE-1 cells, with or without *TINCR* silencing. **C,** Pearson correlation analysis of *TINCR* and *PADI1* expression in 20 NPC tissues. **D,** Statistical analysis results (left) and representative images of DNA electrophoresis (right) for anti-H3K27ac ChIP-PCR in SUNE-1 and HONE-1 cells, with or without *TINCR* silencing. **E,** Western blotting analysis of PADI1, P38 MAPK, p-P38 MAPK, ERK1/2, p-ERK1/2, MMP2, and MMP9 in SUNE1 and HONE1 cells cotransfected with si-*TINCR* or the scrambled control, together with PENTER-*ACLY* or empty vector. **F** and **G,** CCK-8 assays to evaluate the proliferative ability (**F**) or cisplatin sensitivity (**G**) of SUNE-1 and HONE-1 cells cotransfected with si-*TINCR* or the scrambled control, together with PENTER-*ACLY* or empty vector. **H** and **I,** Representative images of migratory (**H**) or invasive (**I**) cells cotransfected with si-*TINCR* or the scrambled control, together with PENTER-*ACLY* or empty vector. Data are presented as the mean ± SD. **, $P < 0.01$. The experiments were repeated independently at least three times.

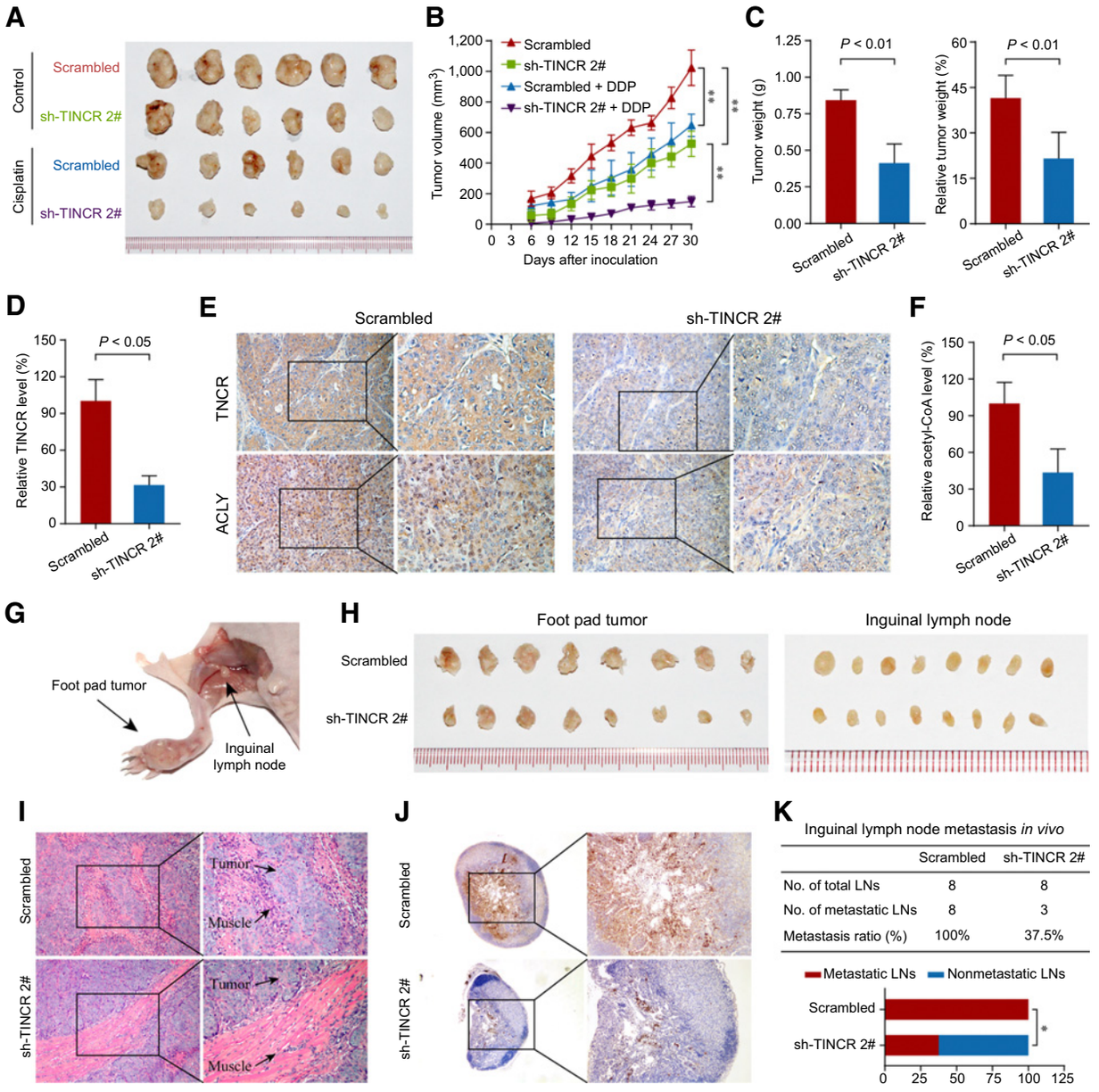

Figure 6.

Silencing *TINCR* impairs NPC proliferation, metastasis, and cisplatin resistances *in vivo*. **A–F,** SUNE-1 cells with or without *TINCR* silencing were transplanted into the axilla of nude mice to construct a tumor growth model. Once the tumor nodes became palpable (~100 mm^3), the mice were randomly divided into four groups ($n = 6$/group) and intraperitoneally injected with normal saline or DDP (4 mg/kg) every 3 days. Representative images (**A**), tumor volume growth curves (**B**), and weight (**C**) of the transplantation tumors. *TINCR* and ACLY expression levels in the above-mentioned tumors were detected using qRT-PCR (**D**), ISH and IHC (**E**). The total acetyl-CoA level of the above-mentioned tumors (**F**). **G–K,** SUNE1 cells, with or without *TINCR* silencing, were injected into the foot pads of mice ($n = 8$/group) to construct inguinal lymph node metastasis models. Representative images of inguinal lymph node metastasis models (**G**), and the primary foot pad tumors and inguinal lymph nodes (**H**). Representative images of the primary foot pad tumors stained with hematoxylin and eosin (**I**), and the inguinal lymph nodes of pan-cytokeratin–positive (above) or –negative (bottom) tumor cells stained by IHC (**J**). Statistical results of the metastatic ratios of inguinal lymph nodes in the scrambled control and *TINCR*-silenced group (**K**). Data are presented as the mean ± SD. *, $P < 0.05$.

Accumulating evidence links the PAD enzyme family with carcinogenesis and tumor progression (51). The *PAD* gene family consists of five members (PAD1–4, 6), which are located within a highly organized gene cluster at 1p36.13, where tumorigenesis-related proteins are predicted to be located (52). In recent years, the PAD enzyme family has gathered increasing attention because of its pivotal role in various cancers. For example, PADI4 mediates citrullination of GSK3β, thereby regulating its nuclear localization and maintaining an epithelial phenotype in breast cancer (53). *PADI2* silencing led to the accumulation of RNAP2 at transcription start sites, thereby

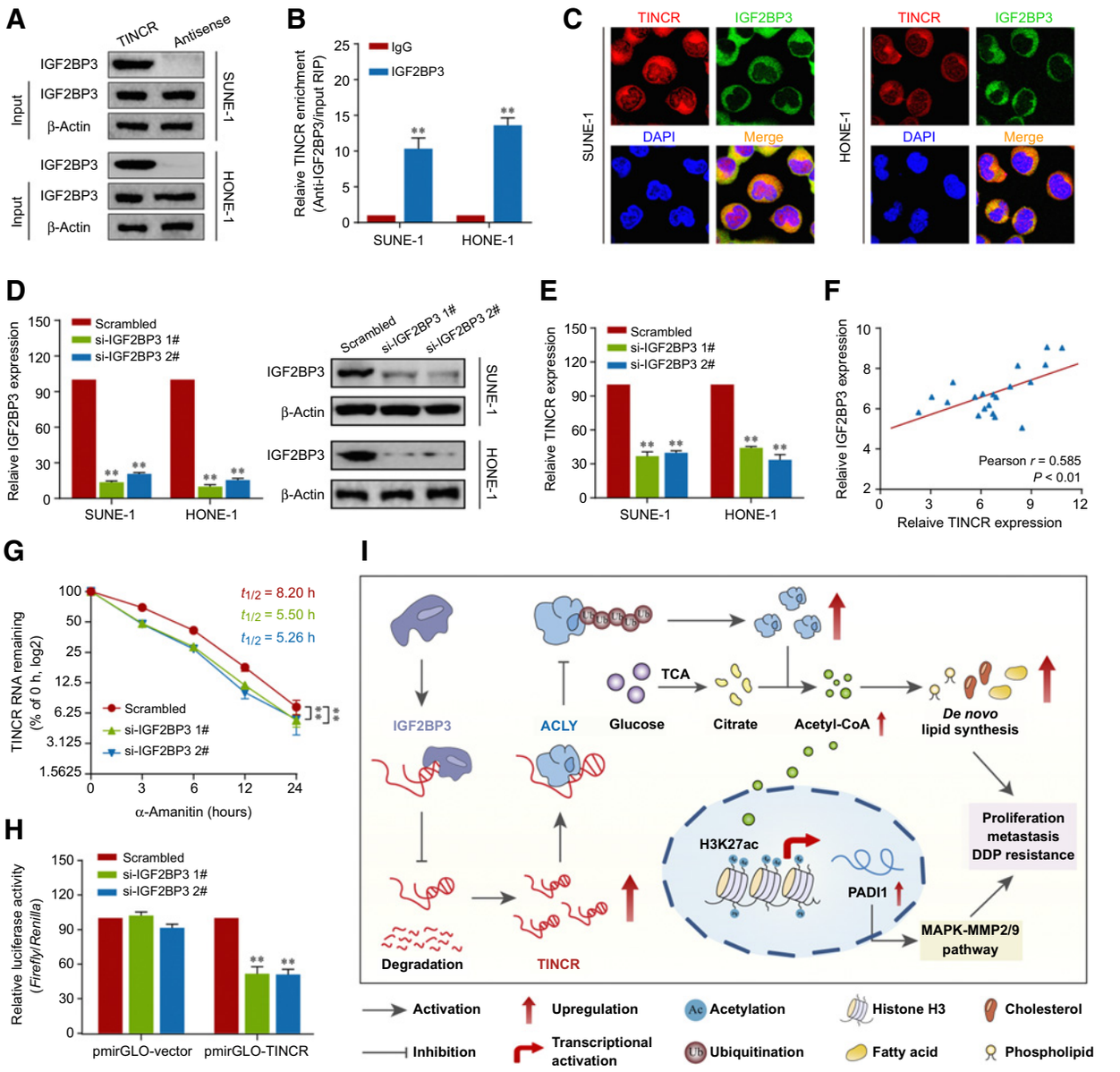

Figure 7.

IGF2BP3 interacts with *TINCR* and slows down its RNA decay. **A,** Western blotting analysis of the interaction of IGF2BP3 and *TINCR* from an RNA pull-down assay using biotin-labeled *TINCR*. **B,** RIP assay was performed using anti-IGF2BP3 antibodies to detect *TINCR* enrichment in the immunoprecipitated complexes. **C,** FISH and IF assays showing that *TINCR* (Cy3; red) and IGF2BP3 (green) are mainly colocalized in the cytoplasm. Nuclei, blue (DAPI). **D,** Quantitative qRT-PCR (left) and Western blotting (right) analysis of *IGF2BP3* expression in SUNE-1 and HONE-1 cells transfected with si*IGF2BP3*s or the scrambled control. **E,** Expression of *TINCR* in SUNE-1 and HONE-1 cells transfected with si*IGF2BP3*s or the scrambled control. **F,** Pearson correlation analysis of *IGF2BP3* and *TINCR* mRNA expression in 20 NPC tissues, determined using qRT-PCR. **G,** The remaining *TINCR* RNA after blocking new RNA synthesis using α-amanitin (50 μmol/L) and normalizing to the 18S rRNA (a product of RNA polymerase I that is unchanged by α-amanitin). **H,** The luciferase activities in SUNE1 cells transfected with the full-length *TINCR* plasmid or empty vector together with si*IGF2BP3*s or the scrambled control. **I,** Proposed model for the mechanism of *TINCR* in promoting NPC proliferation, metastasis, and DDP resistance. Data are presented as the mean ± SD. **, $P < 0.01$. The experiments were repeated independently at least three times.

suppressing target gene expression and inhibiting cell proliferation (54). Moreover, PADI1 promotes epithelial–mesenchymal transition and metastasis via the MAPK–MMP2/9 signaling pathway in breast cancer. Thus, it is conceivable that overexpression of *TINCR* promotes histone acetylation, upregulates *PADI1* expression and promotes NPC progression and cisplatin resistance by regulating the MAPK–MMP2/9 pathway.

Until now, little was known about the general role of RNA decay in the context of cancer. While miRNAs are identified to bind to their target mRNAs and mark them for degradation, we still have a long way

to go before we fully understand the network that controls the stability of a single RNA. In this study, we identified one distinct RBP family gene, *IGF2BP3*, which can interact with *TINCR* and slow down its RNA decay. Human IGF2BP3, initially termed KOC and identified because of its high abundance in pancreatic cancer (55), is proposed to control the translation or turnover of various candidate target transcripts (56). As an oncofetal protein, IGF2BP3 is reported to promote cancer cell proliferation, invasion, and chemoresistance probably by enhancing RNA stability (57). Consistent with previous studies, we found that *IGF2BP3* was upregulated in NPC. Silencing *IGF2BP3* led to accelerated decay of *TINCR*, indicating that the upregulation of *TINCR* in NPC might partially result from the RNA stability function of *IGF2BP3*. However, to promote our understanding of the oncogenic role of IGF2BP3, future studies should focus on how IGF2BP3 enhances a malignant tumor cell phenotype in NPC.

Authors' Disclosures

No disclosures were reported.

Authors' Contributions

Z.-Q. Zheng: Conceptualization, resources, data curation, software, formal analysis, validation, investigation, visualization, methodology, writing-original draft, writing-review and editing. **Z.-X. Li:** Data curation, software, formal analysis, validation, visualization, methodology, writing-original draft, writing-review and editing. **J.-L. Guan:** Data curation, formal analysis, validation, methodology. **X. Liu:** Conceptualization, resources, data curation, investigation. **J.-Y. Li:** Formal analysis, project administration. **Y. Chen:** Conceptualization, resources, supervision, investigation. **L. Lin:** Validation, investigation. **J. Kou:** Conceptualization, resources, data curation. **J.-W. Lv:** Software, supervision, funding acquisition. **L.-L. Zhang:** Formal analysis, validation, visualization. **G.-Q. Zhou:** Funding acquisition, project administration. **R.-Q. Liu:** Conceptualization. **F. Chen:** Validation, investigation. **X.-J. He:** Data curation. **Y.-Q. Li:** Writing-review and editing. **F. Li:** Resources. **S.-S. Xu:** Visualization. **J. Ma:** Supervision, funding acquisition. **N. Liu:** Conceptualization, resources, data curation, supervision, funding acquisition, methodology, writing-original draft, project administration, writing-review and editing. **Y. Sun:** Conceptualization, resources, data curation, supervision, funding acquisition, writing-original draft, project administration, writing-review and editing.

Acknowledgments

This work was supported by grants from the National Natural Science Foundation of China (no. 81872463, 81773229), the Health & Medical Collaborative Innovation Project of Guangzhou City, China (no. 201604020003, 201803040003), the Special Support Program of Sun Yat-sen University Cancer Center (16zxtzlc06), the Natural Science Foundation of Guangdong Province (no. 2017A030312003), the Innovation Team Development Plan of the Ministry of Education (no. IRT_17R110), and the National Key R&D Program of China (2016YFC0902000). The datasets generated and/or analyzed during this study are available at Research Data Deposit public platform (www.researchdata.org.cn), with the approval number of RDDB2019000666.

The costs of publication of this article were defrayed in part by the payment of page charges. This article must therefore be hereby marked *advertisement* in accordance with 18 U.S.C. Section 1734 solely to indicate this fact.

Received November 18, 2019; revised May 22, 2020; accepted October 12, 2020; published first October 16, 2020.

References

1. Bray F, Ferlay J, Soerjomataram I, Siegel RL, Torre LA, Jemal A. Global cancer statistics 2018: GLOBOCAN estimates of incidence and mortality worldwide for 36 cancers in 185 countries. CA Cancer J Clin 2018;68:394–424.
2. Lee AW, Ng WT, Chan LL, Hung WM, Chan CC, Sze HC, et al. Evolution of treatment for nasopharyngeal cancer–success and setback in the intensity-modulated radiotherapy era. Radiother Oncol 2014;110:377–84.
3. Zhang Y, Chen L, Hu GQ, Zhang N, Zhu XD, Yang KY, et al. Gemcitabine and cisplatin induction chemotherapy in nasopharyngeal carcinoma. N Engl J Med 2019;381:1124–35.
4. Peng H, Chen L, Li WF, Guo R, Mao YP, Zhang Y, et al. Tumor response to neoadjuvant chemotherapy predicts long-term survival outcomes in patients with locoregionally advanced nasopharyngeal carcinoma: a secondary analysis of a randomized phase 3 clinical trial. Cancer 2017;123:1643–52.
5. Hanahan D, Weinberg RA. Hallmarks of cancer: the next generation. Cell 2011; 144:646–74.
6. Robey RB, Weisz J, Kuemmerle NB, Salzberg AC, Berg A, Brown DG, et al. Metabolic reprogramming and dysregulated metabolism: cause, consequence and/or enabler of environmental carcinogenesis? Carcinogenesis 2015;36: S203–31
7. Vernieri C, Casola S, Foiani M, Pietrantonio F, de Braud F, Longo V. Targeting cancer metabolism: dietary and pharmacologic interventions. Cancer Discov 2016;6:1315–33.
8. Vernieri C, Casola S, Foiani M, Pietrantonio F, de Braud F, Longo V. Impact of systemic and tumor lipid metabolism on everolimus efficacy in advanced pancreatic neuroendocrine tumors (pNETs). Int J Cancer 2019;44:1704–12.
9. Lee JV, Berry CT, Kim K, Sen P, Kim T, Carrer A, et al. Acetyl-CoA promotes glioblastoma cell adhesion and migration through Ca(2+)-NFAT signaling. Genes Dev 2018;32:497–511.
10. Lin H, Jiang M, Liu L, Yang Z, Ma Z, Liu S, et al. The long noncoding RNA Lnczc3h7a promotes a TRIM25-mediated RIG-I antiviral innate immune response. Nat Immunol 2019;20:812–23.
11. Cai Q, Wang S, Jin L, Weng M, Zhou D, Wang J, et al. Long non-coding RNA GBCDRlnc1 induces chemoresistance of gallbladder cancer cells by activating autophagy. Mol Cancer 2019;18:82.
12. Bester AC, Lee JD, Chavez A, Lee YR, Nachmani D, Vora S, et al. An integrated genome-wide CRISPRa approach to functionalize lncRNAs in drug resistance. Cell 2018;173:649–64.e20.
13. Liao M, Liao W, Xu N, Li B, Liu F, Zhang S, et al. LncRNA EPB41L4A-AS1 regulates glycolysis and glutaminolysis by mediating nucleolar translocation of HDAC2. EBioMedicine 2019;41:200–13
14. Shang C, Wang W, Liao Y, Chen Y, Liu T, Du Q, et al. LNMICC promotes nodal metastasis of cervical cancer by reprogramming fatty acid metabolism. Cancer Res 2018;78:877–90.
15. Wang Y, He L, Du Y, Zhu P, Huang G, Luo J, et al. The long noncoding RNA lncTCF7 promotes self-renewal of human liver cancer stem cells through activation of Wnt signaling. Cell Stem Cell 2015;16:413–25.
16. Zhang Q, Tang Z, An R, Ye L, Zhong B. USP29 maintains the stability of cGAS and promotes cellular antiviral responses and autoimmunity. Cell Res 2020;30: 821–2.
17. Zhong B, Zhang L, Lei C, Li Y, Mao A, Yang Y, et al. The ubiquitin ligase RNF5 regulates antiviral responses by mediating degradation of the adaptor protein MITA. Immunity 2009;30:397–407.
18. Lin C, Miles WO. Beyond CLIP: advances and opportunities to measure RBP–RNA and RNA–RNA interactions. Nucleic Acids Res 2019;47:5490–501.
19. Kargapolova Y, Levin M, Lackner K, Danckwardt S. sCLIP—an integrated platform to study RNA–protein interactomes in biomedical research: identification of CSTF2tau in alternative processing of small nuclear RNAs. Nucleic Acids Res 2017;45:6074–86.
20. Hafner M, Landthaler M, Burger L, Khorshid M, Hausser J, Berninger P, et al. Transcriptome-wide identification of RNA-binding protein and MicroRNA target sites by PAR-CLIP. Cell 2010;141:129–41.
21. Licatalosi DD, Mele A, Fak JJ, Ule J, Kayikci M, Chi SW, et al. HITS-CLIP yields genome-wide insights into brain alternative RNA processing. Nature 2008;456: 464–9.
22. Kopp F, Mendell JT. Functional classification and experimental dissection of long noncoding RNAs. Cell 2018;172:393–407.
23. Schmitt AM, Chang HY. Long noncoding RNAs in cancer pathways. Cancer Cell 2016;29:452–63.

24. Zhang C, Liu J, Huang G, Zhao Y, Yue X, Wu H, et al. Cullin3-KLHL25 ubiquitin ligase targets ACLY for degradation to inhibit lipid synthesis and tumor progression. Genes Dev 2016;30:1956–70.
25. Li Z, Hou P, Fan D, Dong M, Ma M, Li H, et al. The degradation of EZH2 mediated by lncRNA ANCR attenuated the invasion and metastasis of breast cancer. Cell Death Differ 2017;24:59–71.
26. Yang F, Huo XS, Yuan SX, Zhang L, Zhou WP, Wang F, et al. Repression of the long noncoding RNA-LET by histone deacetylase 3 contributes to hypoxia-mediated metastasis. Mol Cell 2013;49:1083–96.
27. Yang F, Zhang H, Mei Y, Wu M. Reciprocal regulation of HIF-1alpha and lincRNA-p21 modulates the Warburg effect. Mol Cell 2014;53:88–100.
28. Granchi C. ATP citrate lyase (ACLY) inhibitors: an anti-cancer strategy at the crossroads of glucose and lipid metabolism. Eur J Med Chem 2018;157: 1276–91.
29. Schug ZT, Vande Voorde J, Gottlieb E. The metabolic fate of acetate in cancer. Nat Rev Cancer 2016;16:708–17.
30. Lu M, Zhu WW, Wang X, Tang JJ, Zhang KL, Yu GY, et al. ACOT12-dependent alteration of acetyl-CoA drives hepatocellular carcinoma metastasis by epigenetic induction of epithelial-mesenchymal transition. Cell Metab 2019;29:886–900.e5.
31. Raisner R, Kharbanda S, Jin L, Jeng E, Chan E, Merchant M, et al. Enhancer activity requires CBP/P300 bromodomain-dependent histone H3K27 acetylation. Cell Rep 2018;24:1722–9.
32. van Roermund CW, Elgersma Y, Singh N, Wanders RJ, Tabak HF. The membrane of peroxisomes in Saccharomyces cerevisiae is impermeable to NAD(H) and acetyl-CoA under *in vivo* conditions. EMBO J 1995;14:3480–6.
33. Comerford SA, Huang Z, Du X, Wang Y, Cai L, Witkiewicz AK, et al. Acetate dependence of tumors. Cell 2014;159:1591–602.
34. Qin H, Liu X, Li F, Miao L, Li T, Xu B, et al. PAD1 promotes epithelial-mesenchymal transition and metastasis in triple-negative breast cancer cells by regulating MEK1-ERK1/2-MMP2 signaling. Cancer Lett 2017;409:30–41.
35. Ren X, Yang X, Cheng B, Chen X, Zhang T, He Q, et al. HOPX hypermethylation promotes metastasis via activating SNAIL transcription in nasopharyngeal carcinoma. Nat Commun 2017;8:14053.
36. Hammerle M, Gutschner T, Uckelmann H, Ozgur S, Fiskin E, Gross M, et al. Posttranscriptional destabilization of the liver-specific long noncoding RNA HULC by the IGF2 mRNA-binding protein 1 (IGF2BP1). Hepatology 2013;58: 1703–12.
37. He J, Zuo Q, Hu B, Jin H, Wang C, Cheng Z, et al. A novel, liver-specific long noncoding RNA LINC01093 suppresses HCC progression by interaction with IGF2BP1 to facilitate decay of GLI1 mRNA. Cancer Lett 2019;450:98–109.
38. Hosono Y, Niknafs YS, Prensner JR, Iyer MK, Dhanasekaran SM, Mehra R, et al. Oncogenic role of THOR, a conserved cancer/testis long non-coding RNA. Cell 2017;171:1559–72.e20.
39. Yuan JH, Liu XN, Wang TT, Pan W, Tao QF, Zhou WP, et al. The MBNL3 splicing factor promotes hepatocellular carcinoma by increasing PXN expression through the alternative splicing of lncRNA-PXN-AS1. Nat Cell Biol 2017;19: 820–32.
40. Tang XR, Li YQ, Liang SB, Jiang W, Liu F, Ge WX, et al. Development and validation of a gene expression-based signature to predict distant metastasis in locoregionally advanced nasopharyngeal carcinoma: a retrospective, multicentre, cohort study. Lancet Oncol 2018;19:382–93.
41. Huarte M. The emerging role of lncRNAs in cancer. Nat Med 2015;21:1253–61.
42. Kretz M. TINCR, staufen1, and cellular differentiation. RNA Biol 2013;10:1597–601.
43. Zheng Y, Yang C, Tong S, Ding Y, Deng W, Song D, et al. Genetic variation of long non-coding RNA TINCR contribute to the susceptibility and progression of colorectal cancer. Oncotarget 2017;8:33536–43.
44. Li CY, Liang GY, Yao WZ, Sui J, Shen X, Zhang YQ, et al. Integrated analysis of long non-coding RNA competing interactions reveals the potential role in progression of human gastric cancer. Int J Oncol 2016;48:1965–76.
45. Zaidi N, Swinnen JV, Smans K. ATP-citrate lyase: a key player in cancer metabolism. Cancer Res 2012;72:3709–14.
46. Zu XY, Zhang QH, Liu JH, Cao RX, Zhong J, Yi GH, et al. ATP citrate lyase inhibitors as novel cancer therapeutic agents. Recent Pat Anticancer Drug Discov 2012;7:154–67.
47. Hatzivassiliou G, Zhao F, Bauer DE, Andreadis C, Shaw AN, Dhanak D, et al. ATP citrate lyase inhibition can suppress tumor cell growth. Cancer Cell 2005;8: 311–21.
48. Braig S. Chemical genetics in tumor lipogenesis. Biotechnol Adv 2018;36:1724–9.
49. Wellen KE, Hatzivassiliou G, Sachdeva UM, Bui TV, Cross JR, Thompson CB. ATP-citrate lyase links cellular metabolism to histone acetylation. Science 2009; 324:1076–80.
50. Pearce NJ, Yates JW, Berkhout TA, Jackson B, Tew D, Boyd H, et al. The role of ATP citrate-lyase in the metabolic regulation of plasma lipids. Hypolipidaemic effects of SB-204990, a lactone prodrug of the potent ATP citrate-lyase inhibitor SB-201076. Biochem J 1998;334:113–9.
51. Alghamdi M, Al GK, Khan RH, Uversky VN, Redwan EM. An interplay of structure and intrinsic disorder in the functionality of peptidylarginine deiminases, a family of key autoimmunity-related enzymes. Cell Mol Life Sci 2019;76: 4635–62.
52. Ellsworth RE, Vertrees A, Love B, Hooke JA, Ellsworth DL, Shriver CD. Chromosomal alterations associated with the transition from in situ to invasive breast cancer. Ann Surg Oncol 2008;15:2519–25.
53. Stadler SC, Vincent CT, Fedorov VD, Patsialou A, Cherrington BD, Wakshlag JJ, et al. Dysregulation of PAD4-mediated citrullination of nuclear GSK3beta activates TGF-beta signaling and induces epithelial-to-mesenchymal transition in breast cancer cells. Proc Natl Acad Sci U S A 2013;110:11851–6.
54. Sharma P, Lioutas A, Fernandez-Fuentes N, Quilez J, Carbonell-Caballero J, Wright R, et al. Arginine citrullination at the C-terminal domain controls RNA polymerase II transcription. Mol Cell 2019;73:84–96.e7.
55. Mueller-Pillasch F, Lacher U, Wallrapp C, Micha A, Zimmerhackl F, Hameister H, et al. Cloning of a gene highly overexpressed in cancer coding for a novel KH-domain containing protein. Oncogene 1997;14:2729–33.
56. Lederer M, Bley N, Schleifer C, Huttelmaier S. The role of the oncofetal IGF2 mRNA-binding protein 3 (IGF2BP3) in cancer. Semin Cancer Biol 2014;29: 3–12.
57. Samanta S, Sharma VM, Khan A, Mercurio AM. Regulation of IMP3 by EGFR signaling and repression by ERbeta: implications for triple-negative breast cancer. Oncogene 2012;31:4689–97.